Journal of Physics D: Applied Physics

PAPER

Mid-infrared adaptive thermal camouflage using a phase-change material coupled dielectric nanoantenna

To cite this article: Ebru Buhara *et al* 2021 *J. Phys. D: Appl. Phys.* **54** 265105

IOP Publishing Journal of Physics D: Applied Physics
J. Phys. D: Appl. Phys. **54** (2021) 265105 (11pp) https://doi.org/10.1088/1361-6463/abf53d

Mid-infrared adaptive thermal camouflage using a phase-change material coupled dielectric nanoantenna

Ebru Buhara[1,2,*], Amir Ghobadi[1,2], Bahram Khalichi[1,2], Hasan Kocer[1] and Ekmel Ozbay[1,2,3,4,*]

[1] NANOTAM-Nanotechnology Research Center, Bilkent University, 06800 Ankara, Turkey
[2] Department of Electrical and Electronics Engineering, Bilkent University, 06800 Ankara, Turkey
[3] Department of Physics, Bilkent University, 06800 Ankara, Turkey
[4] UNAM-Institute of Materials Science and Nanotechnology, Bilkent University, Ankara, Turkey

E-mail: ebru.buhara@bilkent.edu.tr and ozbay@bilkent.edu.tr

Received 18 January 2021, revised 17 March 2021
Accepted for publication 6 April 2021
Published 23 April 2021

Abstract

Recently, camouflage technology has attracted researchers' attention in a large variety of thermal applications. As a special phase change material (PCM), vanadium dioxide (VO_2) is an excellent candidate for the studies conducted on thermal camouflage technology. VO_2 has a transition from the insulator phase to the metal phase with the increase of the temperature. With regards to this unique feature, VO_2 can contribute dynamic properties to the camouflage design. In this paper, a PCM–dielectric based metamaterial mid-infrared adaptive thermal camouflage nanoantenna is designed to perfectly mimic the atmospheric windows. The adaptive property of the proposed structure is obtained by using an ultrathin VO_2 interlayer embedded within the grating. The spectral responses of the structure are computed using the finite difference time domain method, and the invisibility of the structure is proved using power calculations in the different mid-infrared regions.

Keywords: thermal camouflage, mid-infrared, thermal detection, nanoantenna emitter, metamaterial, vanadium dioxide

(Some figures may appear in colour only in the online journal)

1. Introduction

According to Plank's law, objects emit thermal radiation if the temperature of the structure is above absolute zero [1]. This thermal radiation can be calculated by the Stefan–Boltzmann law that indicates the emission from an object is proportional to the fourth power of the temperature (T^4) and the surface emissivity (ε) [2]. To find the surface emissivity, Kirchhoff's law for thermal radiation can be utilized, pointing out that the absorptivity of an object is equal to its emissivity [3]. For an ideal blackbody, which is known as a perfect absorber, the absorptivity therefore the emissivity is unity and, in this case, the radiation will only be dependent on temperature. For other objects, surface emissivity varies from 0 to 1, so the outgoing radiation is a function of both temperature and surface emissivity [4].

Controlling the thermal emission from an object can be accomplished using two different approaches called: (a) temperature control, and (b) surface emissivity control [5]. Compared to the first approach that may require supplementary cooling and heating devices [6], the surface emissivity control is a rather compatible and robust approach to tailoring the thermal emission. Accordingly, the best design to prevent the thermal emission from a hot object in the infrared (IR) region seems to be a highly reflective structure with near-zero

* Authors to whom any correspondence should be addressed.

emission and near-unity reflection covering the interior hot object. However, the blocking of all the wavelengths can cause a thermal imbalance and lead to heat build-up [7]. Instead of suppressing all of the emission spectrum, the surface heat can be selectively emitted in some spectral regions while it is mitigated in other ranges. These regions are determined according to atmospheric windows in the IR wavelengths. Inside the $3-12\,\mu$m spectrum, there are non-transmissive windows with near-zero transmission such as $4-4.2\,\mu$m and $5-8\,\mu$m [8], where the atmospheric gases including N_2, O_2, CO_2, and water vapor can completely absorb the emitted energy, in a relatively short propagation length. In addition, the electromagnetic waves due to thermal radiation can propagate with minimal losses inside the spectrum regions belonging to atmospheric transmissive windows. That is why thermal camera systems that are used for 24/7 all-weather surveillance operate either in the mid-wave IR spectral band ($3-5\,\mu$m) or in the long-wave IR range ($8-12\,\mu$m), while the mid-IR (MIR) camouflage structures are widely designed to operate at the non-transmissive windows to hide from thermal imaging systems and cameras [9–12]. The atmospheric transmission spectrum (T_{atm}) is related to the atmospheric absorption by $\varepsilon_{\text{atm}} = 1 - T_{\text{atm}}$, where they are modeled by considering the US standard atmosphere compositions at the different vertical distances [13].

To reach the desired emission spectrum, metamaterials and metasurfaces made of nano-structured designs are proposed and demonstrated as one of the most effective methods [14–18] to achieve spectrally selective thermal emitters, and to reduce the surface emittance as well as the emitted power from the surfaces. This method constitutes one of the main optical paths used in the thermal camouflage technology where the thermal visibility disappears from the selected working wavelength regions [6] or the emissions in the region of interests are selectively suppressed.

Besides utilizing optical metasurface architectures, thermally tunable active phase change materials (PCMs), such as germanium antimony telluride (GeSbTe or GST) chalcogenide [19–21], perovskite manganese oxide [22], samarium nickel oxide ($SmNiO_3$) [23], and most importantly vanadium dioxide (VO_2) [24], can be used as an ideal scheme to control the thermally tuned optical response. The usage of PCMs with diverse optical properties brings up a unique solution in different technologies [25]. In particular, due to the temperature-dependent optical features of the PCM, these materials are promising candidates for emissivity engineering applications [26–28]. However, the insulator-to-metal transition (IMT) temperatures of the PCMs are the forcing factor that can affect the desired results. For instance, the IMT temperatures of GST and perovskite manganese oxide [21, 22] are around 150 °C and 10 °C, respectively, and $SmNiO_3$ is becomes gradually more metallic from room temperature to 140 °C [23]. Therefore, in our design procedure, VO_2 with an IMT temperature around 68 °C and rapid change around this temperature can be an appropriate choice for the thermal camouflage applications from room temperature to 90 °C [29–32]. Not only that, this matchless switching feature of VO_2 results in various applications, such as IR sensors [33], memristors electronic memories [34], telecommunication modulators [35], and smart windows [36].

The crystal structure of VO_2 in the insulator phase (in the lower temperatures) is a monoclinic, while it turns to tetragonal form and VO_2 dominantly shows metal properties after the temperature of ∼68 °C. Although this transition is reversible and provides adaptivity to the temperature variations [37], a VO_2 thin layer can partially absorb the incident light in its metallic phase without showing any wavelength-selective properties, while the amount of absorption is negligible in the insulator phase. Metamaterials, on the other hand, are selective absorbers with adjustable (narrow/broad) spectral responses [38], but they are passive structures with no temperature sensitivity. Therefore, a hybrid design made of metamaterial absorbers and VO_2 thin films can provide an opportunity to realize spectrally selective active thermal nanoantenna emitters.

In this study, a PCM–dielectric based metasurface nanoantenna emitter design is proposed to achieve low observability at the MIR region by tailoring the spectral emissivity of the design. The proposed thermal nanoantenna emitter is composed of a high index dielectric (silicon (Si) in our case) nanograting on top of a thick silver (Ag) mirror. An ultrathin VO_2 interlayer is embedded within the grating to actively tune its absorption response. The design geometries are adopted to place the resonance wavelengths in the atmospheric absorption windows for thermal camouflage applications. Based on the position of the VO_2 layer, the optical response of the design in the metal phase can be diversely tuned from a narrowband to a broadband thermal emitter. Therefore, upon increase in the surface temperature, the proposed metasurface based thermal nanoantenna emitter turns into a broadband emitter with a stronger radiative thermal emission while it compatibly releases its heat based on the camouflage technology requirement. The proposed design has perfect matching with atmospheric absorption windows so that it can efficiently release its heat without being observed by thermal camera systems. The detectability of the structure by a possible IR sensor is calculated using power calculations over the selected spectra. In addition, due to the hysteresis behavior of VO_2, the calculations are done separately for cooling and heating conditions.

2. Result and discussion

Figure 1(a) is a schematic illustration of the metasurface design, including nanogratings of Si with a constant refractive index of 3.42 on top of Ag resonator (modeling a metallic surface). The spectral refractive index of Ag substrate is taken from the CRC Handbook of Chemistry and Physics [39]. The period, thickness, and width of the Si are set as p, t, and w, respectively. The commercial finite-difference time-domain (FDTD) software package (Lumerical FDTD Solutions) [40] is employed in calculations to seek out optimum geometries and dimensions. These calculations take place in the 2D simulation region, where the incident light propagation direction is chosen as perpendicular to the $x-z$ plane (a uniform plane wave propagating along the $-y$ direction), and the boundary

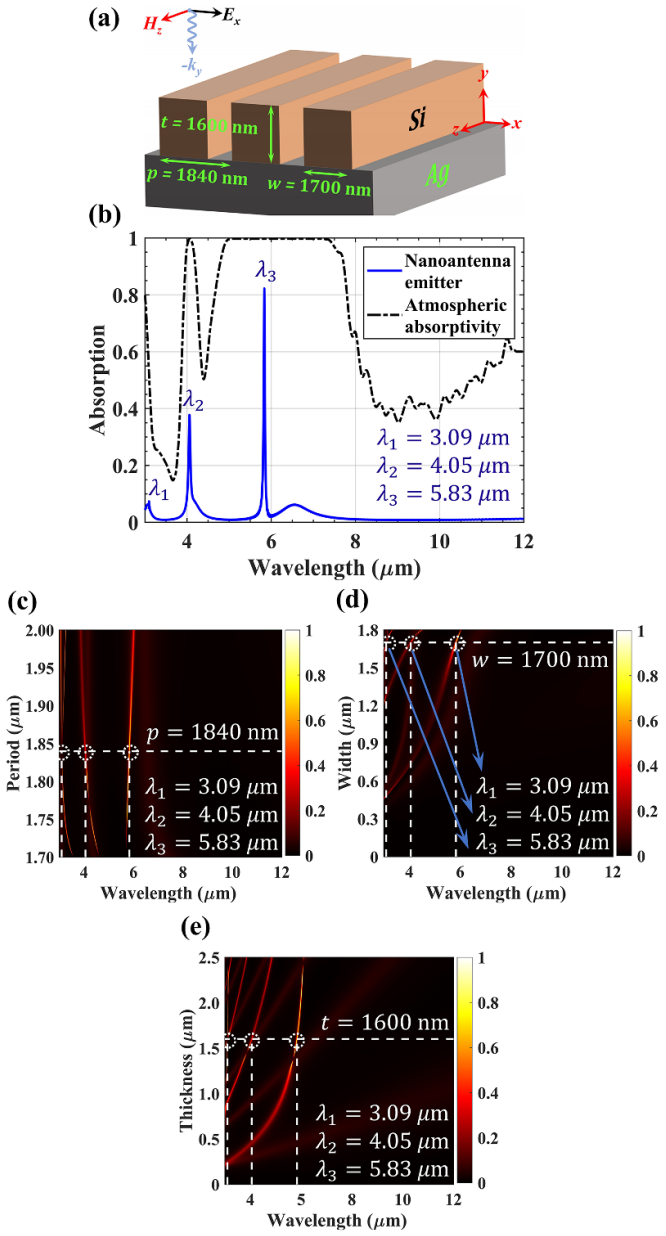

Figure 1. (a) Schematic representation and (b) absorption spectra of the proposed nanoantenna emitter. Impact of the nanograting dimensions including (c) the period, (d) width and (e) thickness on the absorption spectra while each parameter of the structure is kept at its optimized value besides the variation of the target parameter.

conditions for the x direction are chosen as an anti-symmetric boundary and perfectly matched layer for the y direction. A reflection monitor is placed behind the source to integrate the backscattered field, whereas the transmission monitor is located at the front of the source after the structure.

To be invisible to the IR thermal cameras, the resonance peaks of the nanoantenna emitter should be placed in the high absorption regions (atmospheric absorption windows). The design should reflect back the light in the other wavelengths inside the MIR range. Due to the Ag plate in the bottom of the structure, the transmission through the design is small enough to be ignored. Therefore, the only parameter to be considered in the absorption calculation is the reflection spectrum. In the proposed structure, the resonance wavelengths of the absorption spectrum are dependent on the periodicity, width, and thickness of the nanograting. Accordingly, tuning, extending, or shifting of the resonances mainly rely on rational structural design where the geometrical parameters are optimized in such a way that the occurred resonances in the absorption spectrum match the atmospheric absorption windows as presented in figure 1(b). Figures 1(c)–(e) represent the absorptivity versus the wavelength for different geometrical parameters while each parameter of the structure is kept at its optimized value besides the variation of the target parameter. It is observed that three resonances can be excited within the atmospheric absorption windows while the dimensions are selected as $t = 1600$ nm, $w = 1700$ nm, and $p = 1840$ nm.

After the optimization of the design, a VO_2 interlayer is emplaced as shown in figure 2(a). The VO_2 is constructed using experimental refractive index data [24]. The thickness of the plate is set as $t_1 = 10$ nm as a beginning value, and the impact of its position (d_1) inside the grating is studied at both cold (insulator) and hot (metal) states, as shown in figures 2(b) and (c), respectively. The hot state is when the sample is heated up to 90 °C and cold state is the room temperature. From the panel given in figure 2(b), the overall design acts as a narrowband dual absorber in the cold state and the position of VO_2 layer does not change the spectral responses. This is expected by considering the fact that VO_2 has a refractive index close to Si with a small extinction coefficient in the insulator phase. Contrarily, in the hot state, the absorption response drastically changes by moving the position of VO_2 inside the grating where it leads to a broader absorption response as well. All these changes can be more understood by looking at the contour plot given in figure 2(c). At small d_1 values, where the VO_2 layer is in close vicinity of the bottom mirror (design I), the absorption response resembles that of the insulator phase. However, as we move away from the mirror (design II), the bandwidth of the absorption peaks increases. To have a better visualization, the linear plots of the absorption spectra for two different cases of $d_1 = 5$ nm (design I), and $d_1 = 1550$ nm (design II) are plotted in figures 2(d) and (e), respectively. For the $d_1 = 5$ nm case, the spectra for both insulator and metal phases are similar with a slight red shift at the resonance wavelengths. However, in the $d_1 = 1550$ nm case, the absorption peaks at the metal phase have been broadened toward the adjacent wavelength ranges. Therefore, spectral responses can be tailored significantly by the position of the VO_2 interlayer and the transition between the phases. The spectral responses of both designs completely match the atmospheric absorption windows.

In addition, the thickness of the VO_2 interlayer is studied as presented in figures 3(a)–(d). According to figures 3(a) and (c), as the thickness of VO_2 interlayer increases in the insulator phase, and the amount of absorption of design I and design II slightly increase where the second and third resonances are excited efficiently. However, the changes in the insulator phase are not significant enough to affect the thickness decision.

The main factor in the choice of the thickness is the behavior of the resonances in the metal phase for both

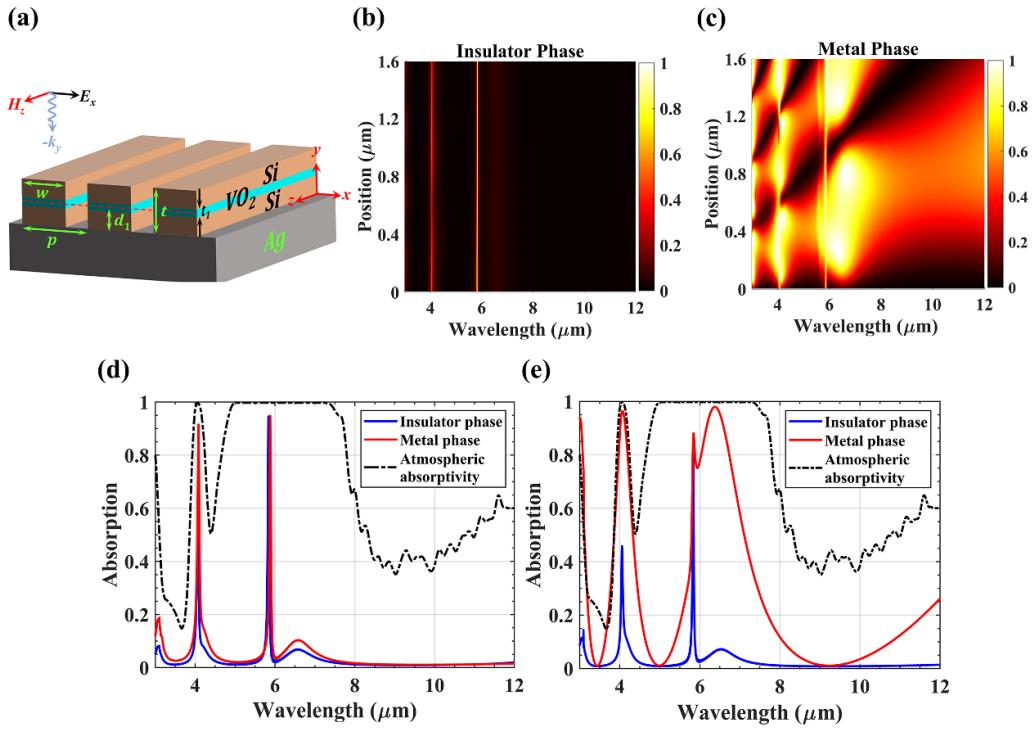

Figure 2. (a) Schematic representation of the PCM–dielectric based metamaterial nanoantenna emitter. The contour plots of the absorption amplitude as a function of VO_2 position for (b) insulator and (c) metal phase conditions. The absorption spectra of the structure in both the metallic and insulator phases for two different VO_2 positions at (d) $d_1 = 5$ nm (design I) and (e) $d_1 = 1550$ nm (design II).

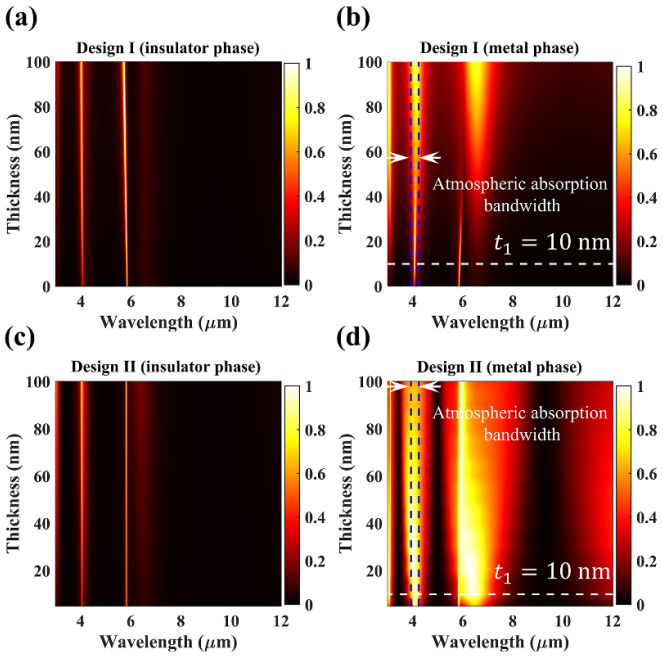

Figure 3. Impact of the VO_2 thickness on the absorption spectrum of design I at (a) the insulator phase, (b) the metallic phase, and on the absorption spectrum of design II at (c) the insulator phase, (d) the metallic phase.

design I and design II, as shown in figures 3(b) and (d). Figure 3(b) demonstrates that increasing the thickness of VO_2 interlayer causes two important changes in the absorption response of design I in the metallic phase. First, the amount of absorption at the third resonance wavelength, as the most important resonance occurred in the main atmospheric absorption window, starts decreasing. Second, in addition to increasing in the amount of absorption at the first and second resonance wavelengths, these resonances are going to be wider which causes the exceeding of the absorption bandwidth of

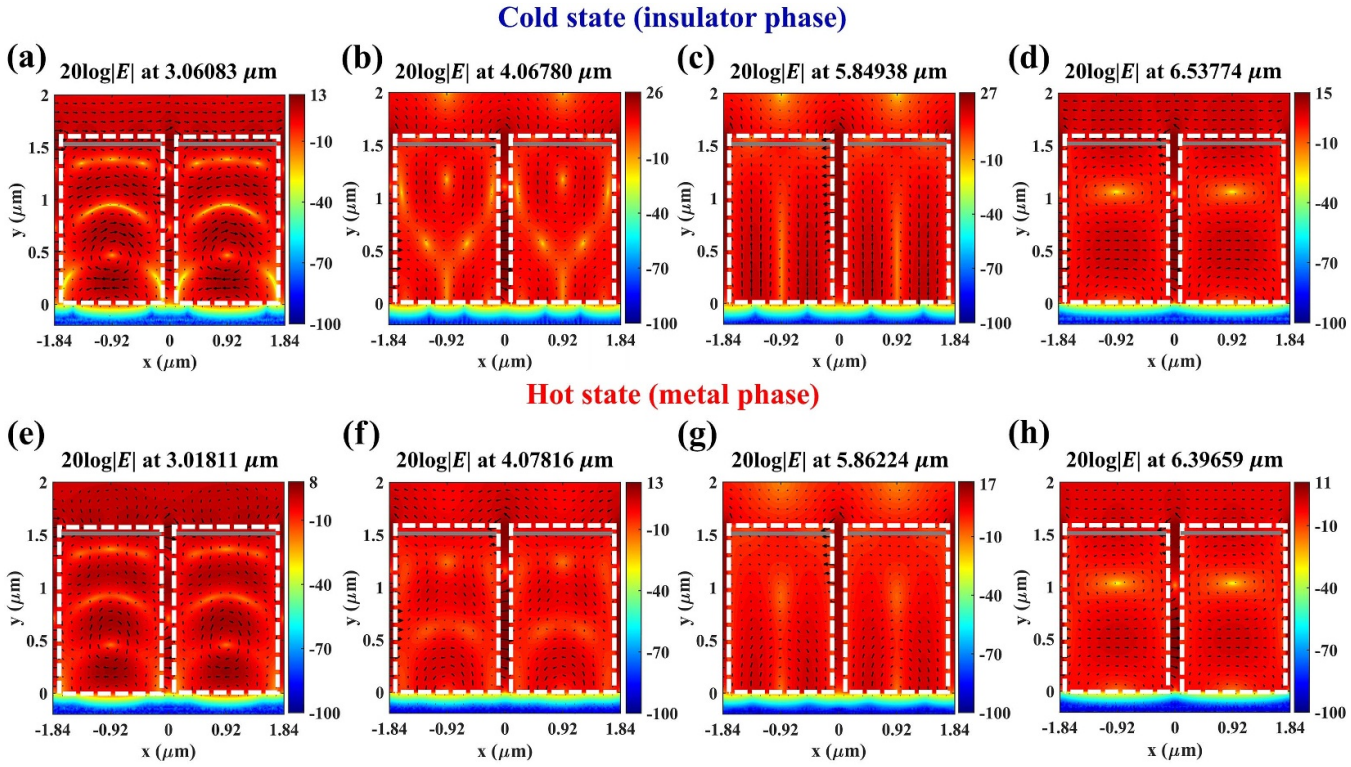

Figure 4. On resonance electric-field distributions across the proposed PCM–dielectric based metamaterial nanoantenna emitter (design II) on the $x-y$ plane for (a)–(d) the cold and (e)–(h) hot states when the position of VO_2 interlayer is $d_1 = 1550$ nm. The color bar is shown in logarithmic scales for better comparison. The thin VO_2 interlayer is shown as the gray lines within the structure while the Si boundaries are shown as white dashed lines.

Table 1. The absorption resonance wavelengths of the proposed PCM–dielectric based metamaterial nanoantenna emitter (design II) at both the metallic and insulator phases when the position of the VO_2 interlayer is $d_1 = 1550$ nm. Relative shifts are calculated based on the division of the differences of the resonances to the resonance occurs at the insulator phase (relative shift $= (\lambda_{\text{metal}} - \lambda_{\text{insulator}})/\lambda_{\text{insulator}}$).

Resonance	#1	#2	#3	#4
Insulator phase	3.06083 μm	4.06780 μm	5.84938 μm	6.53774 μm
Metal phase	3.01811 μm	4.07816 μm	5.86224 μm	6.39659 μm
Relative shift	−0.0139	0.0025	0.0021	−0.02159

the corresponding atmospheric windows. Therefore, using a thicker VO_2 interlayer more than 10 nm is undesirable for design I.

Moreover, as seen in figure 3(d), increasing the thickness of the VO_2 interlayer reduces the amount of absorption and broadens the width of the resonance wavelengths of design II in the metallic phase. The broader response of the second resonance (as a result of thicker VO_2 interlayer) can lead to exceeding the absorption bandwidth of the corresponding atmospheric absorption, which is undesirable. Therefore, similar to the design I, selecting the thickness of VO_2 interlayer around 10 nm can be reasonable and desirable based on the absorption responses of the structure.

To figure out the physical mechanism behind the aforementioned drastic changes, field distribution analyses, and absorbed power density calculations are performed at both metallic and insulator phases of the broadband design (design II). The associated electric-field results on the $x-y$ plane including two periods of the structure are depicted in figures 4(a)–(h). For better visualization, all of the field distributions are shown in the logarithmic scale. The resonance wavelengths of the broadband design for both metallic and insulator cases are also shown in table 1.

As shown in these panels, the electric-field distributions are drastically changed, upon a phase change. In the insulator phase, the on-resonance field profiles (figures 4(b) and (c)) at Ag–Si interface show the excitation of surface plasmons (SPs). Therefore, the grating design triggers the excitation of SPs and this leads to narrowband light absorptions in the resonance wavelengths (see figure 2(e)). However, in the metallic phase (figures 4(f) and (g)), the formation of standing waves can be seen within the grating design. It can be anticipated that the absorption mechanism is dominantly originated from the formation of Fabry–Perot (FP) like cavity

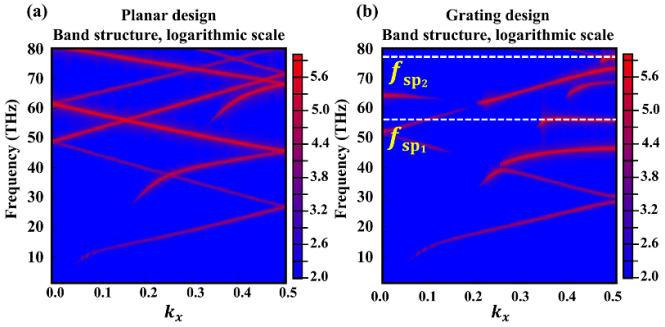

Figure 5. Dispersion diagram of the (a) Ag–Si planar structure and the (b) Ag–Si nanograting structure with the dimensions given in figure 1(a).

resonances. Therefore, in the insulator phase, plasmonic mode is the dominant mechanism while in metallic phase cavity mode is the main absorption mechanism. In fact, moving from lossless insulator phase to lossy metal one, a virtual metal–insulator–metal (MIM) cavity is created in the grating design. This virtual cavity design supports absorption of the light in a broad spectral range. That is the reason behind the broadening of the absorption response. When the VO_2 interlayer is positioned close to the Ag mirror (design I), this MIM cavity cannot be formed, and the resonance profile does not change between two states.

To further investigate mentioned resonances, dispersion relation of the surface waves supported by unpatterned Ag–Si planar structure is calculated by using a band structure technique of the FDTD method. In this band structure technique, a parameter sweep over the transverse wavevector is carried out, and frequencies with strong resonances are searched. Simulated dispersion relation of this multilayer system is shown in figure 5(a). Afterward, the same analysis is performed for the Ag–Si nanograting design, as seen in figure 5(b). Under normal irradiation, SPs cannot be excited in a planar metal–dielectric design, while diffraction by subwavelength nanograting can excite the plasmonic modes. Thus, the differences on dispersion relations of these two structures provide information about the plasmonic modes excited in the nanograting design. As shown by dotted lines in figure 5(b), different from planar structure, two SP frequencies of f_{sp1} and f_{sp2} are present in the nanograting design. The f_{sp1} and f_{sp2} are located at 55 THz ($\lambda = 5.45\,\mu$m) and 76 THz ($\lambda = 3.95\,\mu$m), which are in good agreement with the resonance wavelengths of the Ag–Si nanograting design, presented in figure 1(b).

The above-mentioned statements can be further confirmed by looking at the power absorption profiles across the cavity design on the $x-y$ plane at different resonance wavelengths. The absorbed power density calculations given in figure 6 demonstrate that most of the power is lost inside the Ag substrate at the insulator phase (see figures 6(a) and (b)), while the most partial amount of the absorption at the metallic phase is due to the loss inside the VO_2 interlayer (see figures 6(g) and (h)). This confirms the proposed mechanisms where the dominant absorption in the insulator phase was related to SP excitation on the Ag–Si interface, while it was FP (formation of a virtual MIM lossy cavity) in the metallic phase.

Based on the obtained results, the proposed design (design II) can elegantly modulate its response from a narrowband absorber to a broadband one, upon increasing the temperature. In the meantime, the positions of the absorption resonance wavelengths are adopted in a way to occur within atmospheric absorption windows. This makes the coated object stay invisible to the IR thermal cameras and radiatively cool itself according to Kirchhoff's law. Therefore, the proposed design is an adaptive radiative cooling nanoantenna compatible with thermal camouflage technology.

To verify this capability, emitted power density from the structure is calculated using thermal emission modeling [24]. The model is demonstrated in figure 7(a). First, due to utilizing a thick layer of Ag as a substrate, the transmission can be ignored, and the surface emissivity can be taken as an absorptivity. Therefore, the surface emissivity can be written as;

$$\varepsilon_{\text{eff}}(T,\lambda) = \varepsilon_{\text{structure}}(T,\lambda) = 1 - R_{\text{structure}}(T,\lambda), \qquad (1)$$

where $\varepsilon_{\text{structure}}(T,\lambda)$ and $R_{\text{structure}}(T,\lambda)$ are considered as the absorptivity and reflectivity of the proposed nanoantenna emitter dependent on the operating wavelength (λ) and absolute temperature (T) of the body. Then, the blackbody radiation can be calculated by the formula given by [41];

$$\text{BB}(T,\lambda) = \frac{2\pi hc^2}{\lambda^5}\left(e^{\frac{hc}{\lambda k_B T}} - 1\right)^{-1}, \qquad (2)$$

where h, c, and k_B are Planck constant, the speed of light in vacuum, and Boltzmann constant. The thermal emission can be obtained as a multiplication of (1) by (2) as;

$$\text{TE}(T,\lambda) = \varepsilon_{\text{eff}}(T,\lambda) \times \text{BB}(T,\lambda). \qquad (3)$$

Taking an integral with respect to the wavelengths over the region of interest will give the detected optical power density by the camera as presented in (4);

$$P = \int_{\lambda_2}^{\lambda_1} \text{TE}(T,\lambda)\, d\lambda. \qquad (4)$$

In this work, the wavelength intervals are chosen as $3-4\,\mu$m, $4-4.2\,\mu$m, $4.2-5\,\mu$m, $5-8\,\mu$m and $8-12\,\mu$m according to the atmospheric windows over the $3-12\,\mu$m. The calculated detected power densities for the proposed narrowband structure (design I) are presented in figures 7(b)–(f) in the logarithmic scale. Due to the hysteresis behavior of VO_2 around the transition temperature 68 °C, the heating behavior from insulator to metal and cooling behavior from metal to insulator takes different paths in the transition. To make sure the design has thermal camouflage in both cases, the calculations are done separately for cooling and heating conditions. The intervals $4-4.2\,\mu$m and $5-8\,\mu$m are the regions of interest that the power emission should be high enough for releasing

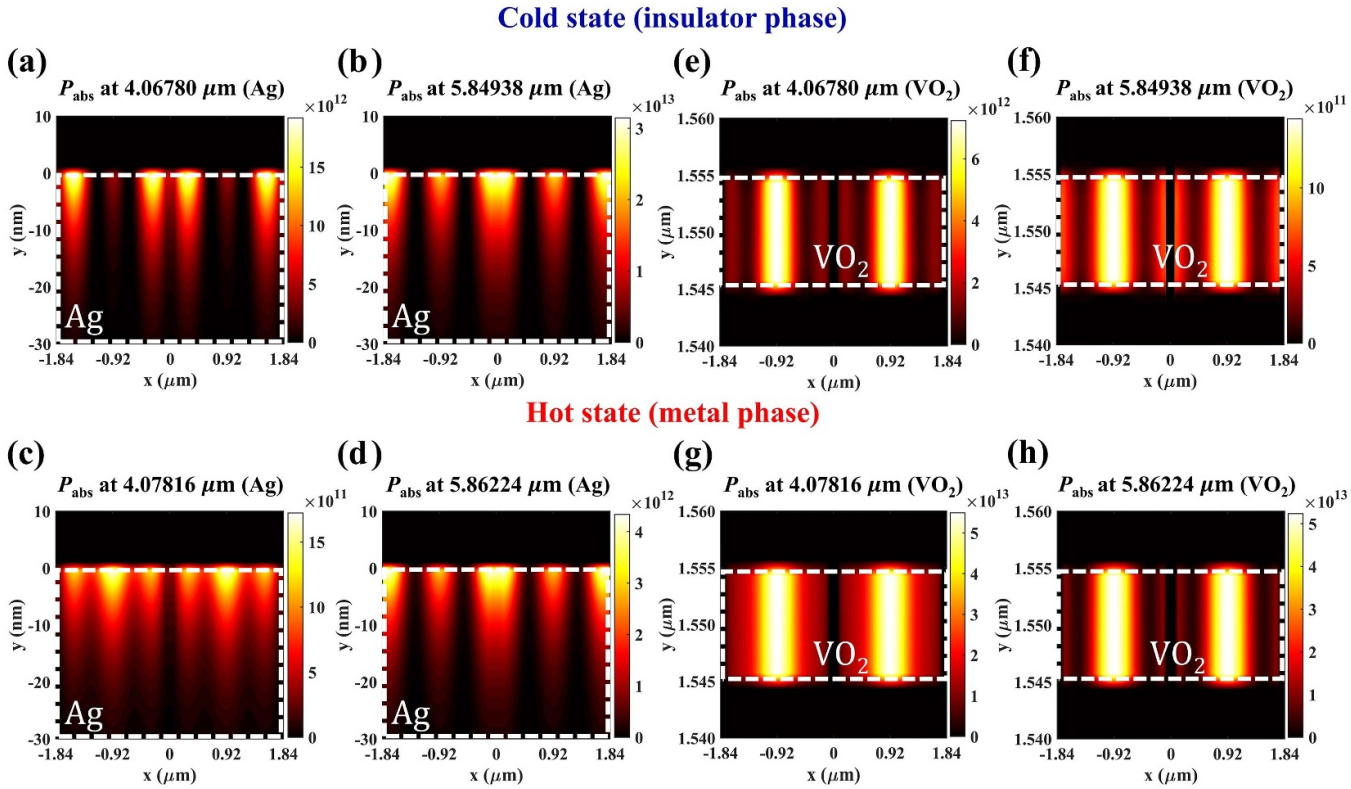

Figure 6. On resonance absorbed power density distributions across the Ag layer on the $x-y$ plane considering two periodicities for (a), (b) the cold and (c), (d) hot states when the position of VO_2 interlayer is $d_1 = 1550$ nm. On resonance absorbed power density distributions across the VO_2 layer on the $x-y$ plane considering two periodicities for (e), (f) the cold and (g), (h) hot states when the position of VO_2 interlayer is $d_1 = 1550$ nm.

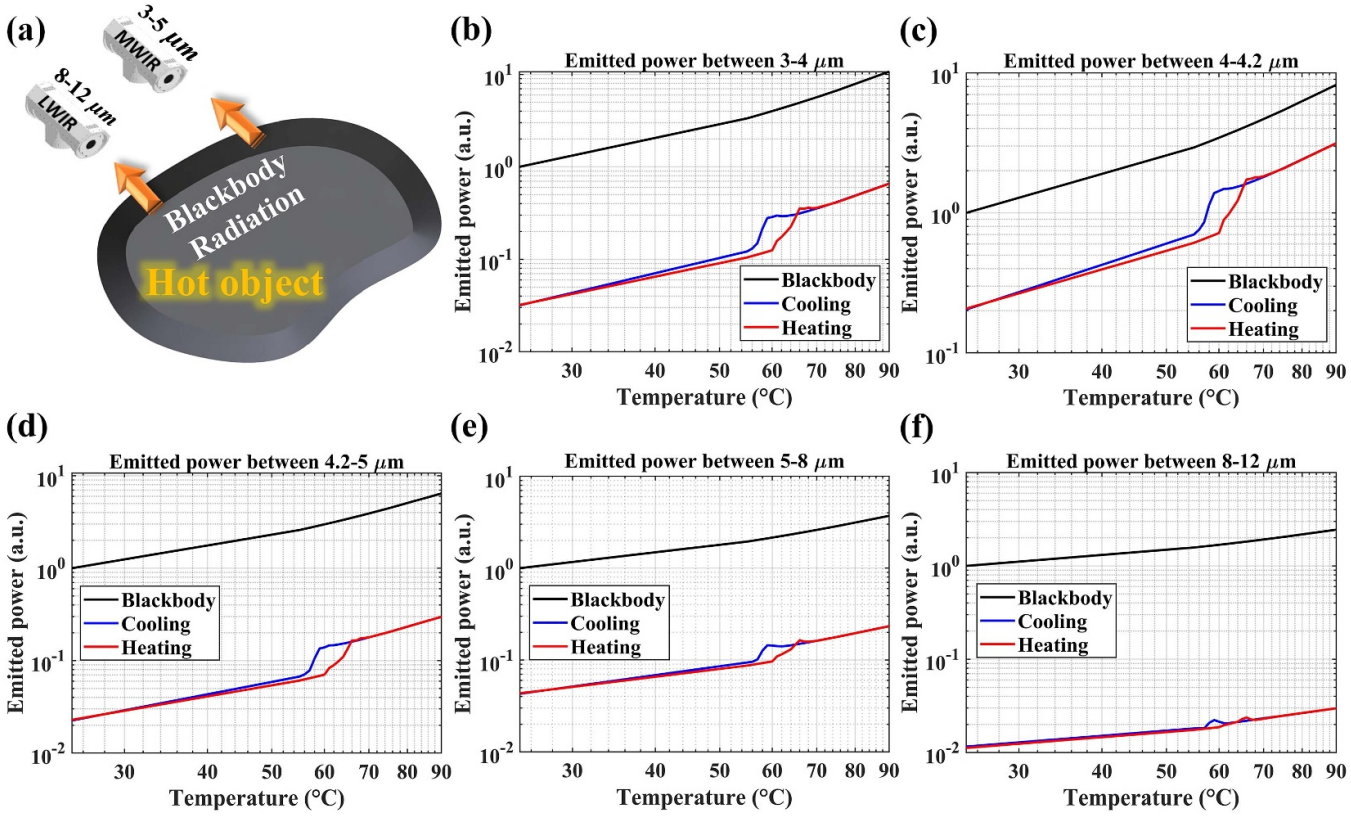

Figure 7. (a) Schematic illustration of the detected optical power density using IR thermal cameras emitted from the proposed PCM–dielectric based metamaterial nanoantenna emitter. Emitted power density calculations of design I given in a logarithmic scale for different intervals including (b) $3-4$ μm, (c) $4-4.2$ μm, (d) $4.2-5$ μm, (e) $5-8$ μm, and (f) $8-12$ μm.

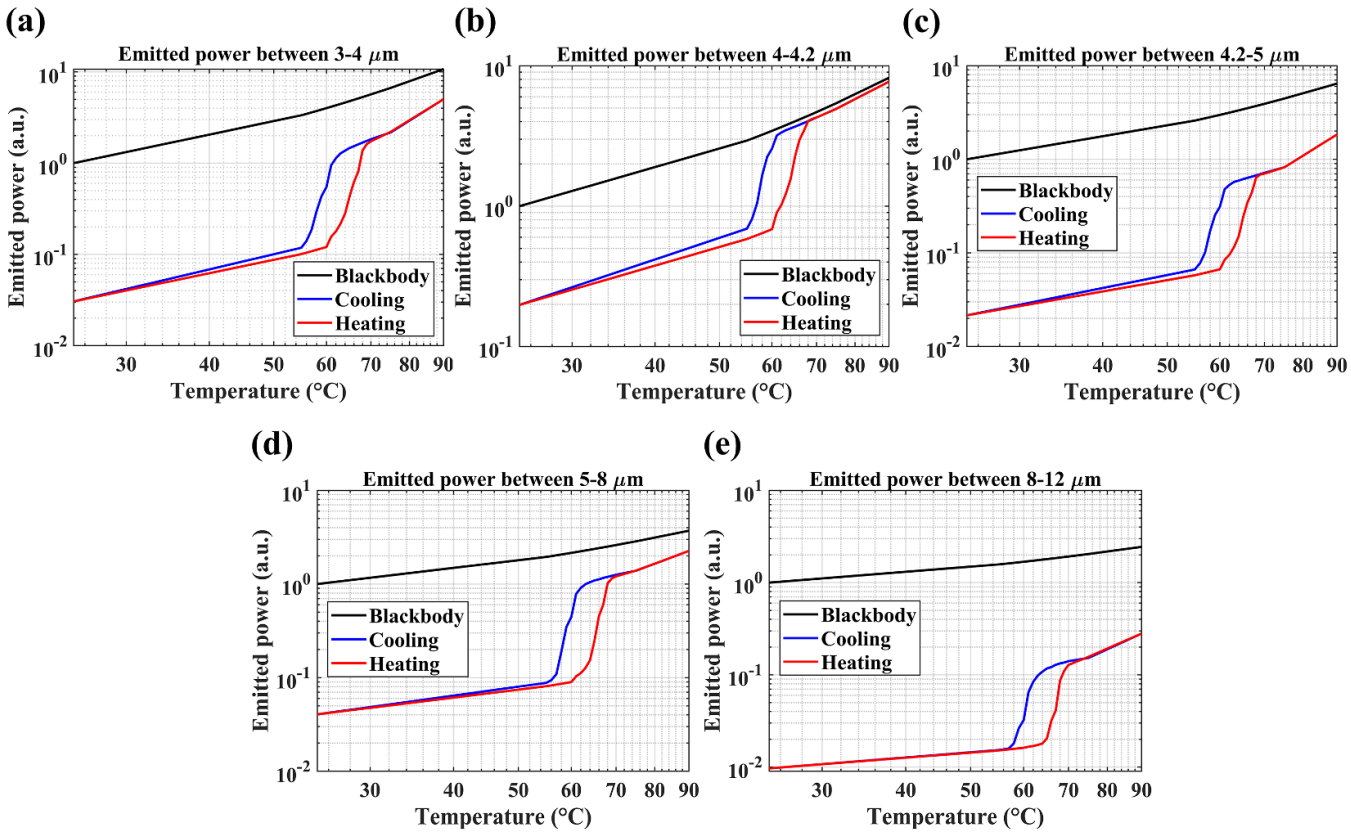

Figure 8. Emitted power density calculations of design II given in a logarithmic scale for different intervals including (a) $3-4\ \mu$m, (b) $4-4.2\ \mu$m, (c) $4.2-5\ \mu$m, (d) $5-8\ \mu$m, and (e) $8-12\ \mu$m.

the energy. In those regions, the released power is expected to be as close as possible to the blackbody radiation so the build-up energy can be released without causing any risk of detection by the IR thermal cameras (see figures 7(c) and (e)). On the contrary, the rest of the intervals are the ones that the atmospheric windows allow the emission of power. Therefore, any power released in those regions should be as small as possible and far away enough from the blackbody radiation for both cooling and heating conditions that can be observed in figures 7(b), (d), and (f).

As discussed before, if the placement of the VO_2 interlayer is arranged to the top part of the Si (design II), the absorption response of the structure at the cold state (insulator phase) will remain almost the same with design I (both designs have similar absorption responses in the insulator phase, see the blue lines in figures 2(d) and (e)). However, the hot state (metallic phase) of design II results in response change from the narrowband to the broadband one. The broadband response means a larger thermal power release. Although the resonance peaks become broader in the hot state, they still stay in the atmospheric absorption windows to prevent any detection probability by the IR thermal cameras. The calculations of the detected powers by an IR camera in a logarithmic scale for the proposed broadband structure (design II) are presented in figures 8(a)–(e). Figures 8(a), (c), and (e) are the calculated powers in the non-absorptive intervals where the powers should place as far as possible from the blackbody radiation. On the other hand, figures 8(b) and (d) are the regions where the response of the design should be close to the blackbody radiation.

The absorption responses and, therefore, the emission responses of the proposed structure, which are placed over the blackbody radiation, for both narrowband and broadband designs (design I and II) in the cold and hot states of the VO_2 interlayer are demonstrated in figure 9. For a better comparison, blackbody radiations at 25 °C and 90 °C, the emission responses of the proposed designs over the blackbody radiations at four different cases, and real emissions of the proposed designs with consideration of atmospheric transmission spectrum are presented. Both narrowband and broadband responses are quite similar in the cold state (see figures 9(a) and (c)). Even though sharp emission peaks are displayed around $6\,\mu$m, the absorption feature of the atmosphere at that wavelength cancels the aforementioned peak in the real emission and, therefore, the design becomes invisible in the MIR region for both designs in the cold state. For the hot state, the emissions over the blackbody demonstrate different peaks for the narrowband and broadband designs (see figures 9(b) and (d)). However, consideration of the atmospheric absorption windows cancels most of the emission and invisibility of the design is preserved. It is observed that narrowband design acts better in comparison to broadband design for thermal camouflage applications but being a perfect and broadband absorber within the absorption windows helps more to reduce

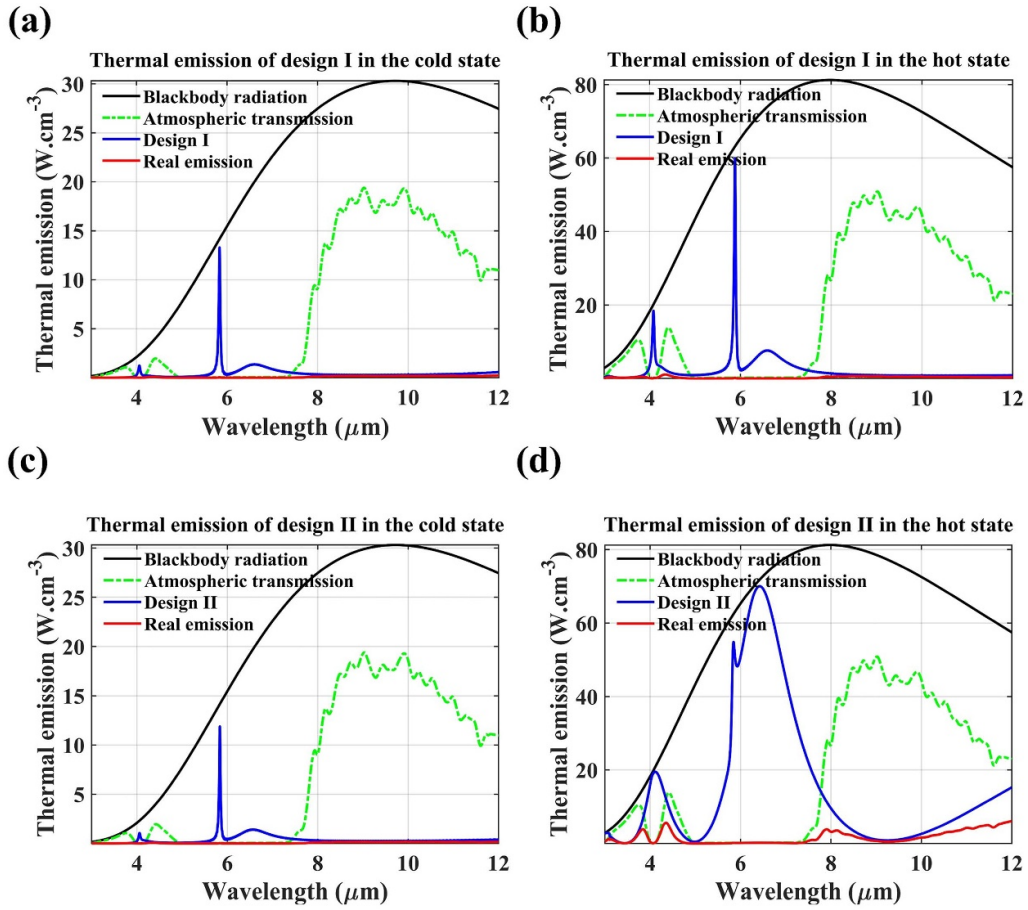

Figure 9. Comparisons among the emitted power densities at different temperatures including blackbody radiation (black solid line), atmospheric transmissivity for 5 km long transmission path through the atmosphere at the ground level (green dashed-dotted line) over the corresponding blackbody radiation, the proposed structure without considering atmospheric transmissivity (blue solid line) over the corresponding blackbody radiation, and the real emission response of the proposed design I and II (red solid line). The emitted power densities of the proposed narrowband design at the (a) cold state when the temperature is 25 °C and (b) hot state when the temperature is 90 °C. The emitted power densities of the proposed broadband design at the (c) cold state when the temperature is 25 °C and (d) hot state when the temperature is 90 °C.

the coated targets' temperature. This leads to thermal balance and radiative heat exchange between the target and low temperature surrounding.

3. Conclusion

This study demonstrates a thermally tunable nanoantenna emitter based on a hybrid design made of a metamaterial absorber and VO_2 thin film as a PCM for thermal camouflage applications. The camouflage capability of the proposed design is in-depth studied using numerical analyses. It was found that an ultrathin VO_2 embedded layer can significantly tailor the antenna response. In the cold state, the absorption response is not VO_2 position dependent and the dominant harvesting mechanism is due to the excitation of plasmonic mode formed in the metal–dielectric interface. On the other hand, the response in the hot state can be effectively manipulated from narrowband (design I) to broadband (design II) by changing the position of the VO_2 thin film. However, in both cases, we adopt a design that is precisely matched the atmospheric absorption windows. Thus, this tunable nanoantenna emitter releases its heat energy into the atmosphere through the absorption windows in the spectrum. The power emission suppression is achieved only at the atmospheric windows and the verification of this behavior is demonstrated with the emitted power calculations over the selected intervals for both narrowband (design I) and broadband (design II) responses. Due to the hysteresis behavior of the VO_2, the calculations are carried out separately under cooling and heating conditions. Calculated power densities demonstrate the superiority of the proposed designs for being utilized in the thermal camouflage applications.

Data availability statement

All data that support the findings of this study are included within the article (and any supplementary files).

ORCID iDs

Ebru Buhara https://orcid.org/0000-0001-7060-7316

Amir Ghobadi https://orcid.org/0000-0002-8146-0361
Bahram Khalichi https://orcid.org/0000-0002-9465-1044
Hasan Kocer https://orcid.org/0000-0003-4107-3014

References

[1] Planck M 1901 Ueber das Gesetz der Energieverteilung im Normalspectrum *Ann. Phys., Lpz.* **309** 553–63
[2] Stefan J 1879 Uber die Beziehung zwischen der Warmestrahlung und der Temperatur, Sitzungsberichte der mathematisch-naturwissenschaftlichen Classe der kaiserlichen *Akad. Wiss.* **79** 391–428
[3] Kirchhoff G 1978 Über das Verhältnis zwischen dem Emissionsvermögen und dem Absorptionsvermögen der Körper für Wärme und Licht *Von Kirchhoff Bis Planck: Theorie Der Wärmestrahlung in Historisch-kritischer Darstellung* ed H-G Schöpf (Wiesbaden: Vieweg+Teubner Verlag) Reihe Wissenschaft pp 131–51
[4] Baranov D G, Xiao Y, Nechepurenko I A, Krasnok A, Alù A and Kats M A 2019 Nanophotonic engineering of far-field thermal emitters *Nat. Mater.* **18** 920–30
[5] Zhu H, Li Q, Zheng C, Hong Y, Xu Z, Wang H, Shen W, Kaur S, Ghosh P and Qiu M 2020 High-temperature infrared camouflage with efficient thermal management *Light Sci. Appl.* **9** 60
[6] Pan M, Huang Y, Li Q, Luo H, Zhu H, Kaur S and Qiu M 2020 Multi-band middle-infrared-compatible camouflage with thermal management via simple photonic structures *Nano Energy* **69** 104449
[7] Kim T, Bae J-Y, Lee N and Cho H H 2019 Hierarchical metamaterials for multispectral camouflage of infrared and microwaves *Adv. Funct. Mater.* **29** 1807319
[8] Zeyghami M, Goswami D Y and Stefanakos E 2018 A review of clear sky radiative cooling developments and applications in renewable power systems and passive building cooling *Sol. Energy Mater. Sol. Cells* **178** 115–28
[9] Xu C, Stiubianu G T and Gorodetsky A A 2018 Adaptive infrared-reflecting systems inspired by cephalopods *Science* **359** 1495–500
[10] Baranwal N and Mahulikar S P 2016 Infrared signature of aircraft engine with choked converging nozzle *J. Thermophys. Heat Transfer* **30** 854–62
[11] Xie X, Li X, Pu M, Ma X, Liu K, Guo Y and Luo X 2018 Plasmonic metasurfaces for simultaneous thermal infrared invisibility and holographic illusion *Adv. Funct. Mater.* **28** 1706673
[12] Phan L, Walkup W G, Ordinario D D, Karshalev E, Jocson J-M, Burke A M and Gorodetsky A A 2013 Reconfigurable infrared camouflage coatings from a cephalopod protein *Adv. Mater.* **25** 5621–5
[13] Berk A, Conforti P, Kennett R, Perkins T, Hawes F and van Den B J 2014 MODTRAN® 6: a major upgrade of the MODTRAN® radiative transfer code *2014 6th Workshop on Hyperspectral Image and Signal Processing: Evolution in Remote Sensing (WHISPERS)* pp 1–4
[14] Qu Y, Li Q, Cai L, Pan M, Ghosh P, Du K and Qiu M 2018 Thermal camouflage based on the phase-changing material GST *Light Sci. Appl.* **7** 26
[15] Xiao L *et al* 2015 Fast adaptive thermal camouflage based on flexible VO_2/graphene/CNT thin films *Nano Lett.* **15** 8365–70
[16] Kats M A, Blanchard R, Zhang S, Genevet P, Ko C, Ramanathan S and Capasso F 2013 Vanadium dioxide as a natural disordered metamaterial: perfect thermal emission and large broadband negative differential thermal emittance *Phys. Rev.* X **3** 041004
[17] Qu Y, Li Q, Du K, Cai L, Lu J and Qiu M 2017 Dynamic thermal emission control based on ultrathin plasmonic metamaterials including phase-changing material GST *Laser Photonics Rev.* **11** 1700091
[18] Buhara E, Ghobadi A and Ozbay E 2020 An all-dielectric metasurface coupled with two-dimensional semiconductors for thermally tunable ultra-narrowband light absorption *Plasmonics* 1–8
[19] Abdollahramezani S *et al* 2021 Dynamic hybrid metasurfaces *Nano Lett.* **21** 1238–45
[20] Abdollahramezani S, Hemmatyar O, Taghinejad H, Krasnok A, Kiarashinejad Y, Zandehshahvar M, Alu A and Adibi A 2020 Tunable nanophotonics enabled by chalcogenide phase-change materials *Nanophotonics* **9** 1189–241
[21] Guo P, Sarangan A M and Agha I 2019 A review of germanium-antimony-telluride phase change materials for non-volatile memories and optical modulators *Appl. Sci.* **9** 530
[22] Fan D, Li Q, Xuan Y, Tan H and Fang J 2013 Temperature-dependent infrared properties of Ca doped (La, Sr)MnO_3 compositions with potential thermal control application *Appl. Therm. Eng.* **51** 255–61
[23] Shahsafi A *et al* 2019 Temperature-independent thermal radiation *Proc. Natl Acad. Sci. USA* **116** 26402–6
[24] Kocer H, Cakir M C, Durna Y, Soydan M C, Odabasi O, Isik H, Aydin K and Ozbay E 2021 Exceptional adaptable MWIR thermal emission for ordinary objects covered with thin VO_2 film *J. Quant. Spectrosc. Radiat. Transfer* **262** 107500
[25] Cesarini G, Leahu G, Belardini A, Centini M, Li Voti R and Sibilia C 2019 Quantitative evaluation of emission properties and thermal hysteresis in the mid-infrared for a single thin film of vanadium dioxide on a silicon substrate *Int. J. Therm. Sci.* **146** 106061
[26] Wang X, Cao Y, Zhang Y, Yan L and Li Y 2015 Fabrication of VO_2-based multilayer structure with variable emittance *Appl. Surf. Sci.* **344** 230–5
[27] Hołyńska M, Tighe A and Semprimoschnig C 2018 Coatings and thin films for spacecraft thermo-optical and related functional applications *Adv. Mater. Interfaces* **5** 1701644
[28] Ba C O F, Bah S T, D'Auteuil M, Fortin V, Ashrit P V and Vallée R 2014 VO_2 thin films based active and passive thermochromic devices for energy management applications *Curr. Appl Phys.* **14** 1531–7
[29] Kalantari Osgouei A, Hajian H, Khalichi B, Serebryannikov A E, Ghobadi A and Ozbay E 2021 Active tuning from narrowband to broadband absorbers using a sub-wavelength VO_2 embedded layer *Plasmonics* 1–9
[30] Morin F J 1959 Oxides which show a metal-to-insulator transition at the neel temperature *Phys. Rev. Lett.* **3** 34–36
[31] Liu D, Ji H, Peng R, Cheng H and Zhang C 2018 Infrared chameleon-like behavior from VO_2 (M) thin films prepared by transformation of metastable VO_2 (B) for adaptive camouflage in both thermal atmospheric windows *Sol. Energy Mater. Sol. Cells* **185** 210–7
[32] Ke Y, Wang S, Liu G, Li M, White T J and Long Y 2018 Vanadium dioxide: the multistimuli responsive material and its applications *Small* **14** 1802025
[33] Gurvitch M, Luryi S, Polyakov A and Shabalov A 2009 Nonhysteretic behavior inside the hysteresis loop of VO_2 and its possible application in infrared imaging *J. Appl. Phys.* **106** 104504
[34] Novodvorsky O A, Parshina L S, Lotin A A, Mikhalevsky V A, Khramova O D, Cherebylo E A and

Ya P V 2018 Vanadium- and titanium dioxide-based memristors fabricated via pulsed laser deposition *J. Surf. Invest.* **12** 322–7

[35] Cueff S, Li D, Zhou Y, Wong F J, Kurvits J A, Ramanathan S and Zia R 2015 Dynamic control of light emission faster than the lifetime limit using VO_2 phase-change *Nat. Commun.* **6** 8636

[36] Kim K-S, Son E-W, Youn J W and Kim D U 2019 Intense pulsed light sintering of vanadium dioxide nanoparticle films and their optical properties for thermochromic smart window *Mater. Des.* **176** 107838

[37] Cakir M C, Kocer H, Durna Y, Yildirim D U, Ghobadi A, Hajian H, Aydin K, Kurt H, Saglam N and Ozbay E 2020 Unveiling the optical parameters of vanadium dioxide in the phase transition region: a hybrid modeling approach *RSC Adv.* **10** 29945–55

[38] Yildirim D U, Ghobadi A, Soydan M C, Atesal O, Toprak A, Caliskan M D and Ozbay E 2019 Disordered and densely packed ITO nanorods as an excellent lithography-free optical solar reflector metasurface *ACS Photonics* **6** 1812–22

[39] Lide D R 2004 *CRC Handbook of Chemistry and Physics* 85th edn (Boca Raton, FL: CRC Press)

[40] Ansoft Lumerical Solutions FDTD 3D Electromagnetic Simulator (www.lumerical.com/products/)

[41] Planck M 2013 *The Theory of Heat Radiation* (New York: Courier Corporation)